

Physics of Cardiac Arrhythmogenesis

Alain Karma

Physics Department and Center for Interdisciplinary Research on Complex Systems, Northeastern University, Boston, Massachusetts 02115; email: a.karma@neu.edu

Annu. Rev. Condens. Matter Phys. 2013. 4:313–37

The *Annual Review of Condensed Matter Physics* is online at conmatphys.annualreviews.org

This article's doi:
10.1146/annurev-conmatphys-020911-125112

Copyright © 2013 by Annual Reviews.
All rights reserved

Keywords

cardiac arrhythmias, excitable media, spiral waves, scroll waves, turbulence, fibrillation, defibrillation, alternans, discordant alternans, nonlinear dynamics, pattern formation, feedback control

Abstract

A normal heartbeat is orchestrated by the stable propagation of an excitation wave that produces an orderly contraction. In contrast, wave turbulence in the ventricles, clinically known as ventricular fibrillation (VF), stops the heart from pumping and is lethal without prompt defibrillation. I review experimental, computational, and theoretical studies that have shed light on complex dynamical phenomena linked to the initiation, maintenance, and control of wave turbulence. I first discuss advances made to understand the precursor state to a reentrant arrhythmia where the refractory period of cardiac tissue becomes spatiotemporally disordered; this is known as an arrhythmogenic tissue substrate. I describe observed patterns of transmembrane voltage and intracellular calcium signaling that can contribute to this substrate, and symmetry breaking instabilities to explain their formation. I then survey mechanisms of wave turbulence and discuss novel methods that exploit electrical pacing stimuli to control precursor patterns and low-energy pulsed electric fields to control turbulence.

1. INTRODUCTION

During a normal heartbeat, an electrical wave that originates in the sinoatrial node (the heart's natural pacemaker) spreads through the heart conduction system (Figure 1a) to produce an orderly contraction of the two atria and then the two ventricles. A sequence of such beats is a normal sinus rhythm (NSR) in a standard electrocardiogram (ECG) (Figure 1b). In contrast, a typical ECG of a patient in a cardiac intensive care unit during an episode of sudden

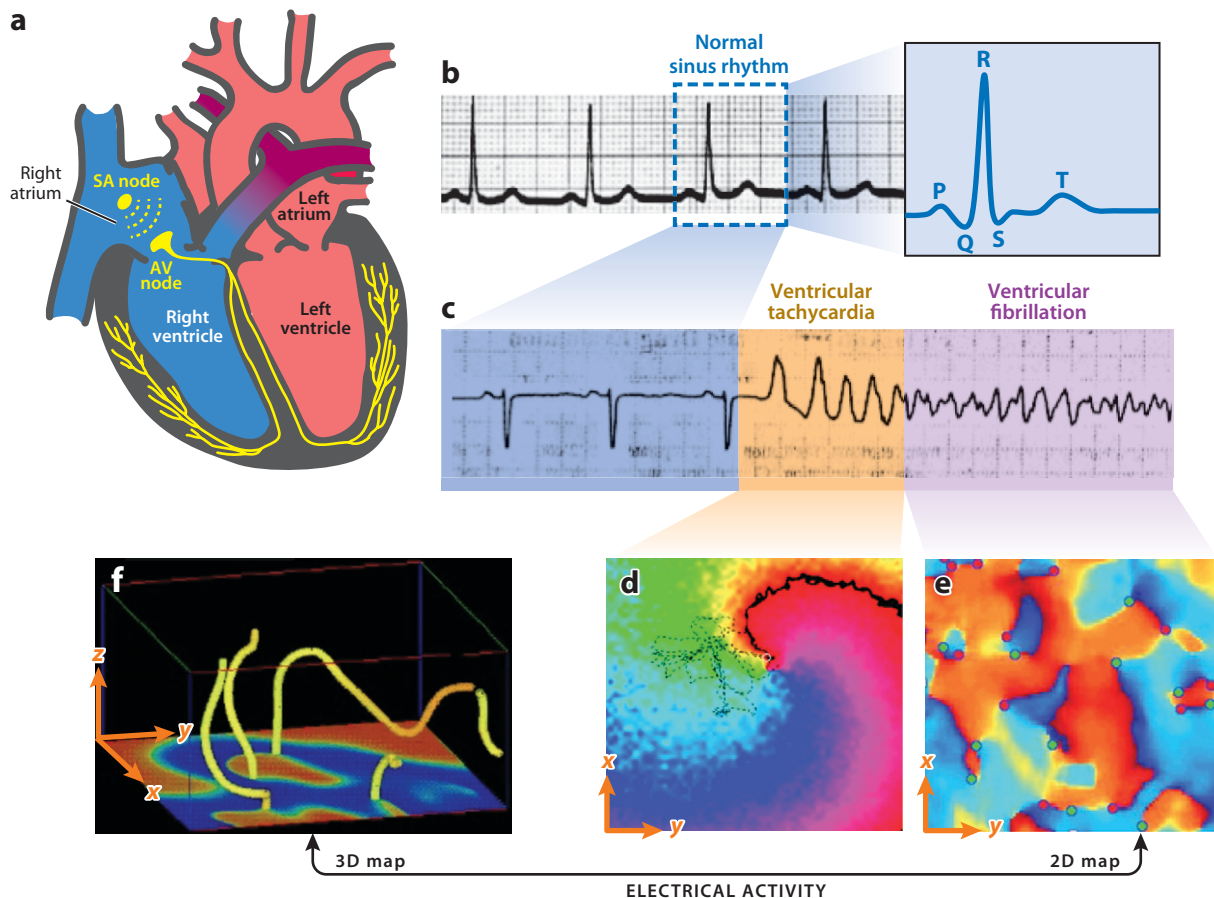


Figure 1

Overview of cardiac arrhythmogenesis. (a) Schematic representation of the heart conduction system where a normal excitation wave originating in the sinoatrial node propagates through the atria, and then through a specialized conduction pathway to the ventricles. (b) ECG of normal sinus rhythm (NSR) associated with atrial contraction (P-wave), ventricular depolarization (QRS complex), and ventricular repolarization (T-wave). (c) ECG of a patient in an intensive care unit illustrating the transition from NSR to ventricular tachycardia (VT) to ventricular fibrillation (VF). (d) Example of a spiral wave in a two-dimensional cardiac tissue culture represented by a colored map of intracellular calcium concentration (courtesy of Emilia Entcheva and Harold Bien). (e) Example of wave turbulence with multiple reentrant circuits at the epicardial surface of a dog's fibrillating left ventricle (courtesy of Eberhard Bodenschatz). Shown is a colored map of the phase θ of voltage excitation waves varying from 0 to 2π . Equation 2 yields $\pm 2\pi$ around phase singularities pinpointed by solid circles of two different colors for clockwise and counterclockwise rotation of reentrant waves. (f) Illustration of vortex filament turbulence in a 3D ionic model simulation of a slab of ventricular tissue with anisotropic conduction (104). The bottom surface, which is analogous to the 2D surface typically imaged experimentally in panel e (as indicated by the bottom arrow), shows a colored map of transmembrane voltage and only the vortex filaments, which are 3D extensions of phase singularities, are represented inside the slab.

cardiac arrest (**Figure 1c**) illustrates that this NSR can abruptly transition to ventricular tachycardia (VT), a more rapid contraction of the ventricles, and then to ventricular fibrillation (VF). During VF, different regions of the heart contract asynchronously, causing the heart surface to quiver with the appearance of randomly twitching fibrils. The resulting loss of heart pumping function is almost always fatal and leads to sudden cardiac arrest, which causes over 300,000 adult deaths each year in the United States. This makes sudden cardiac arrest responsible for half of all heart disease deaths and the largest cause of natural death in the United States.

Key to interpreting the ECG of this patient is the fact that the heart is an excitable medium, a term used to describe spatially extended nonlinear systems that possess a linearly stable resting state, but exhibit an abrupt response to an external stimulus. This includes physical systems such as chemical reactions (1–3) and other living systems such as *Xenopus* eggs (4) and amoeba colonies (5, 6). Those systems exhibit similar wave behaviors, and in particular rotating spiral-shaped waves, also known as rotors, which extend in 3D into scroll waves rotating around a central vortex filament. Once created, those waves are self-sustained and overtake the entire medium if their frequency is higher than any other sources of waves. This is because colliding excitation wavefronts annihilate like forest fire fronts. Advances in optical mapping (7) and computer simulations have led to striking images of spiral waves in cardiac tissue as illustrated in **Figures 1d,e** (see also Reference 8 for a review), largely confirming the hypothesis (3) that those waves play a key role in fibrillation (9–17).

Rotating spiral waves reenter the same region of cardiac tissue more than once, as opposed to only once during a normal heartbeat. For this reason, they are commonly referred to as reentrant waves in the medical literature and the term reentry is used more generally to describe wave circulation as a spiral vortex (functional reentry) or around an obstacle (anatomical reentry). Heart spirals rotate typically at 5–10 Hz and hence completely suppress the heart pacemaker rhythm. VT typically transitions to VF, a more complex form of spiral wave turbulence with annihilation and creation of chaotically moving spirals (**Figure 1e**). Spiral waves also play a role in atrial fibrillation, which is the most common arrhythmia in clinical practice.

A large research activity in the biomedical and physics communities during the past two decades has focused on three sets of questions related to the initiation, maintenance, and control of reentrant arrhythmias:

1. Initiation. For the initiation of VT and VF, a central question is what causes the abrupt dynamical transition from a periodic wave train to a spiral wave attractor? Moreover, what mechanisms facilitate the initiation of reentry in a diseased heart, and how do the initiation mechanisms differ for different diseases? It is well appreciated that localized patches with a prolonged refractory period can block propagation, thereby creating an arrhythmogenic substrate. This substrate can then interact with triggers, abnormal focal sources of waves, to initiate wavebreaks and reentry. Within this traditional conceptual framework of trigger-substrate interaction, the central questions then become the following: What produces an arrhythmogenic substrate, and what causes those triggers?

2. Maintenance. The issue of the maintenance of fibrillation stems from the fact that a generic excitable system such as the Belousov-Zhabotinsky (BZ) reaction supports either rigidly rotating or meandering spiral waves (1), i.e., spiral waves with a tip that traces out flower-like patterns due to a generic core instability (18–22) also seen in some cardiac tissue experiment (dashed line in **Figure 1e**), but not wave turbulence. This raises the questions of what makes

cardiac tissue special as an excitable medium that supports turbulence, and what is the nature of this turbulence?

3. Control. For the control of reentrant arrhythmias, the key questions are the following: How can the initiation of reentry be prevented, and how can turbulence be suppressed after it occurs? Drug therapies that target molecular components of the heart's electrical circuitry to suppress triggers and/or reduce the arrhythmogenicity of the substrate are attractive but have so far been ineffective and unreliable. Therefore, how to manipulate pacing stimuli or low-energy electrical shocks to control arrhythmias, as an alternative to high-intensity electrical shocks used by current defibrillators, is a practically important question.

The next section briefly discusses the physics of cardiac excitation waves and reviews basic mechanisms of trigger-substrate interaction that provide the conceptual framework to address the questions in the sections that follow. The last section summarizes the main advances and outlines future challenges.

2. BACKGROUND

2.1. Physics of Cardiac Excitation Waves

Ionic mechanisms of nerve impulse propagation were elucidated in pioneering experimental studies of the giant squid axon conducted by Hodgkin and Huxley (HH), who also provided a mathematical framework to describe this propagation. Similar mechanisms govern electrical excitation in heart tissue, and extensions of the HH equations have been developed over the years to incorporate a growing amount of cardiac electrophysiological data (23–28). Pedagogical expositions of the HH formalism can be found in textbooks (e.g., see Reference 29). Extensions of the HH formalism to the heart and more microscopic models have been reviewed recently in Reference 30. Only a few necessary ingredients are summarized in this section and later in Section 3.4, when discussing excitation-contraction coupling.

At the smallest molecular scale, the generation of electrical impulse is governed by the flow of ions through ion channels embedded in the cell membrane (**Figure 2a**). Those channels have selective permeabilities to different ions, principally Na^+ , K^+ , and Ca^+ in heart cells, and different currents contribute to different phases of the cardiac action potential (AP), which refers to the nonlinear excursion of the transmembrane voltage V_m [the difference $V_m = V_e - V_i$ between the extracellular (V_e) and intracellular (V_i) potentials] in response to an electrical stimulus (**Figure 2b**). The total ionic current per unit area of membrane is the sum of the whole-cell ionic currents for the different channel types $I_{ion} = I_{Na} + I_{Ca,L} + I_{Kr} + I_{Ks} + I_{K1} + I_{NCX} + \dots$. The cell membrane is a lipid bilayer impermeable to the flow of ions that can hold a charge difference across the membrane. The electrical circuit for a heart cell is therefore this capacitor and a conductor carrying a total current (I_{ion}) in parallel. Conservation of charge for this circuit yields the equation $dV_m/dt = -(I_{ion} + I_{ext})/C_m$, where I_{ext} is the externally applied current, and C_m is the capacitance. The heart's natural pacemaker cells located in the sinoatrial node (**Figure 1a**) are spontaneously oscillatory and generate an electrical signal without this external current. However, the vast majority of cells in the atria and ventricles are excitable and require external stimulation to generate an action potential when studied in isolation.

In cardiac tissue (**Figure 2c**), cells are electrically coupled by ion flow from cell to cell, intracellularly through gap junctional proteins localized at cell junctions, and extracellularly through interstitial spaces. Consequently, a one-dimensional row of cardiac cells can be described by an analog circuit (**Figure 2d**). Applying Kirchhoff's law to each node of this circuit and

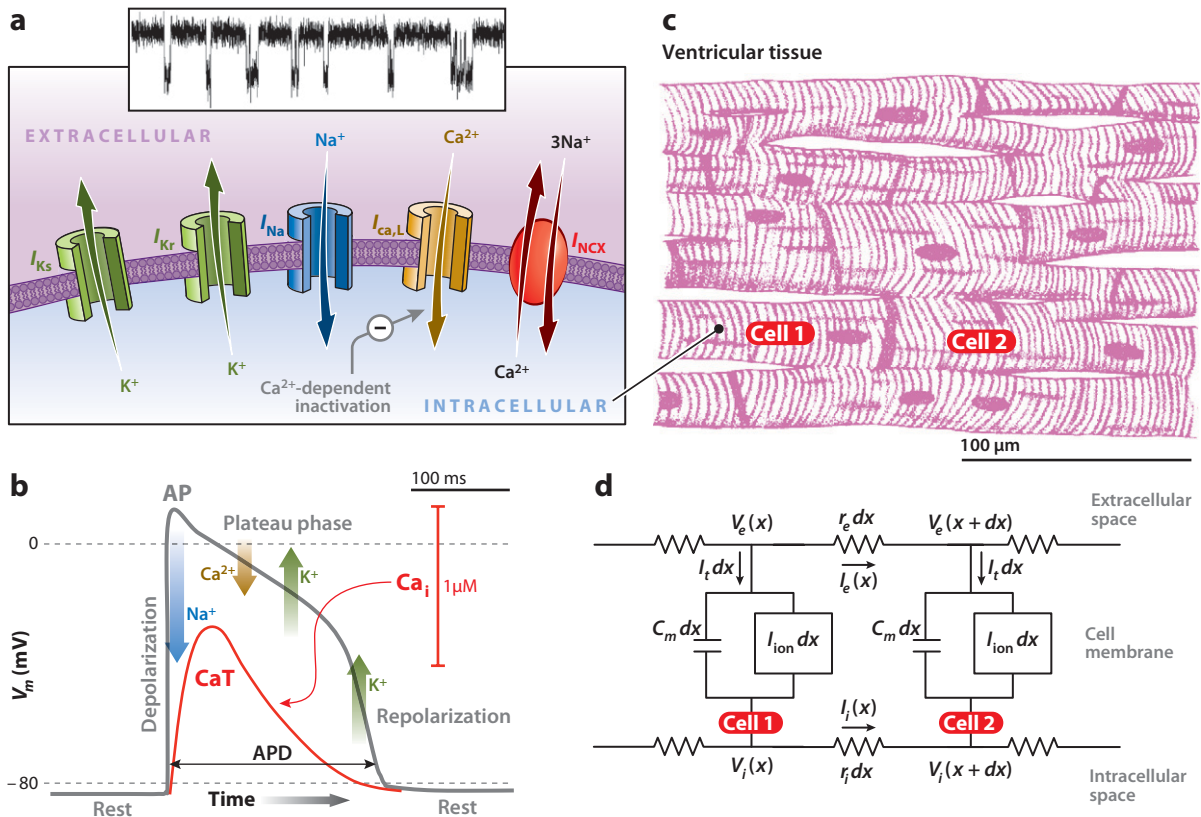


Figure 2

Ionic mechanisms and electrical circuitry underlying cardiac excitation wave propagation. (a) Schematic representation of the outer sarcolemmal membrane of the ventricular cell incorporating ion channels with selective permeabilities to different ions. The illustration at the top is a typical patch clamp recording of the current through a single ion channel that exhibits stochastic transitions between closed and open states. This single channel current is typically of the order of picoampere, and transitions between states take place on a millisecond timescale. This channel noise is almost completely averaged out at the whole-cell level due to the large number (a few thousands) of channels of each type. (b) Contributions of various ionic currents to the cardiac action potential (AP) representing the time course of transmembrane voltage V_m in response to a suprathreshold electrical stimulus, and a calcium transient (CaT) representing the rise of intracellular cytosolic Ca concentration Ca_i that activates the cell contractile machinery. (c) Schematic representation of cardiac tissue where ions can pass from cell to cell through gap junctional proteins located at cell junctions and also flow in extracellular spaces. (d) Circuit analog of cardiac tissue used to derive the cable equation (Equation 1) for AP propagation.

taking the continuum limit $V_m(x - dx) + V_m(x + dx) - 2V_m(x) \approx \partial_x^2 V_m dx^2$ yields the cable equation

$$\partial_t V_m = D_V \partial_x^2 V_m - (I_{ion}(V_m; \dots) + I_{ext}) / C_m, \quad 1.$$

where $D_V = 1/[2\pi a(r_i + r_e)C_m]$ is the voltage diffusion coefficient; a is the cell radius; and the resistances r_i and r_e are defined per unit length of cable in **Figure 2d**, whereas C_m is defined per area (per length $\times 2\pi a$) of membrane. Pacing stimuli are delivered by the external current I_{ext} applied at one point, which mimics the sinoatrial node and produces waves of AP that propagate with a self-preserving shape. All the complexity of cardiac electrophysiology is buried in $I_{ion}(V_m; \dots)$ in Equation 1. In the traditional HH formalism, the dots denote functional

dependencies of individual currents on gate variables that control highly nonlinear time-dependent changes of ionic conductances in response to changes of V_m . Dynamical equations derived from fits to experimentally measured currents that must be solved together with Equation 1 govern these gates. These equations describe the collective effect, at the whole-cell level, of microscopic transitions of ion channels between closed, inactivated, or open conducting states. In addition, the intracellular Ca^{2+} ion concentration Ca_i rises transiently during electrical excitation (**Figure 1b**) to activate the cell contractile machinery (31, 32). Ca_i directly influences several ionic currents and can have an arrhythmogenic role. Hence, more recent ionic models also typically include Ca_i dynamics treated as a single dynamical variable at the whole-cell level (28, 33) or spatially distributed inside the cell in more elaborate models (34–37).

More microscopic Markov models (29, 30) attempt to describe channel states based on stochastic single-channel current recordings that capture these transitions (**Figure 2a**, top). Because there are a few thousand ion channels of a given type in a cell, the summation of such recordings produces an essentially deterministic whole-cell current. Therefore, channel noise is typically negligible, except close to bifurcations where it can play an especially important role in the generation of spontaneous excitation waves via mechanisms involving voltage (38–41) or calcium (42, 43) dynamics. The most biologically realistic models have become extremely complex, with many interacting molecular components, but simpler models with a few variables already capture many important properties of excitable waves (see, e.g., Reference 44 and earlier references therein).

2.2. Topological Defects and Trigger-Substrate Interactions

Spiral waves can be viewed as topological defects, similar to edge dislocations of a solid or vortices of a superfluid or superconductor. These defects can be characterized by defining a phase variable θ from a phase portrait of any pair of variables $(u(\vec{r}, t), v(\vec{r}, t))$ that can adequately describe the cardiac excitation cycle, such as $(V_m(\vec{r}, t), Ca_i(\vec{r}, t))$, or $(V_m(\vec{r}, t + \tau), V_m(\vec{r}, t))$ where τ is a fixed delay. Irrespective of the choice of variables, phase portraits are closed loops in the (u, v) plane, and $\theta(\vec{r}, t)$ can be defined as the polar coordinate of the point $(u(\vec{r}, t), v(\vec{r}, t))$ with respect to an arbitrary fixed origin inside this loop.

This phase varies generally smoothly in space, except at spiral centers where the phase is singular, as illustrated in **Figure 1e**, which shows a spatial map of θ varying from 0 to 2π during VF. Similarly to a Burgers circuit for dislocations, one can define the topological charge of a spiral wave from a contour integral:

$$\oint \vec{\nabla} \theta \cdot \vec{d}l = \pm 2\pi \text{ or } 0, \quad 2.$$

which yields $\pm 2\pi$ if a spiral tip lies inside the contour, with the sign giving its rotation direction (clockwise or counterclockwise), or zero otherwise. Topological charge is conserved except through boundary effects so that spirals generally need to be created or annihilated in pairs.

Winfree proposed a conceptual pinwheel experiment to explain the formation of phase singularities by a high-intensity electrical stimulus (45). **Figure 3a** is a 2D simulation of a simple ionic model of this experiment. It consists of exciting the entire left edge of a tissue with a first stimulus (labeled S1), thereby generating a rightward propagating planar wave, and then delivering after some delay a second point stimulus (labeled as S2) at the center of the tissue. The effect of the S2 stimulus depends on timing. If it is delivered long after the passage of the plane wave, it depolarizes a circular region of tissue and creates an extra, albeit benign, excitation wave that propagates to

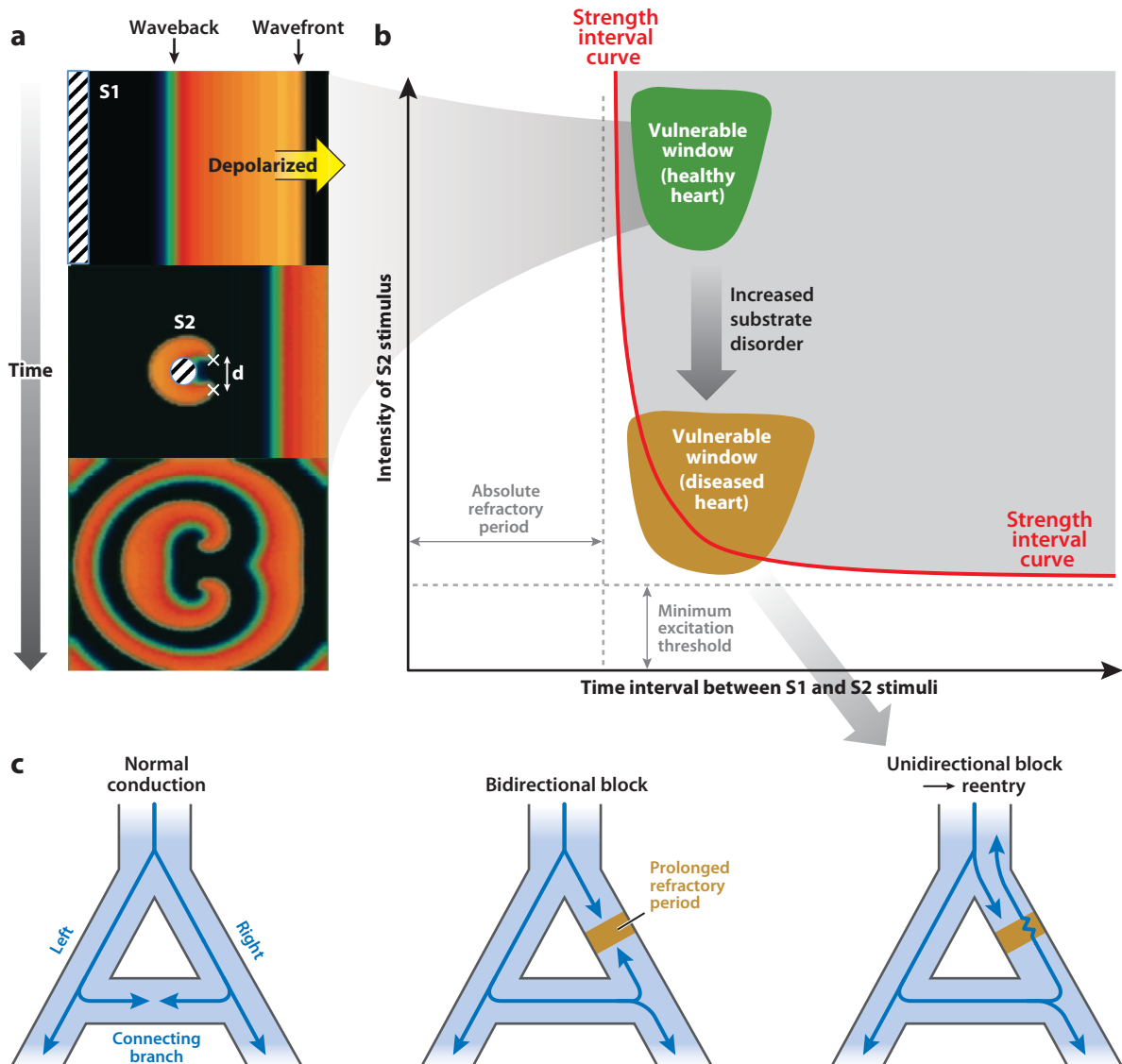


Figure 3

Illustration of trigger-substrate interactions underlying the vulnerable window for the initiation of reentrant arrhythmias. (a) Computer simulations in 2D tissue illustrating the initiation of two phase singularities (white crosses) and figure-of-eight reentry by an S2 stimulus inside the vulnerable window with time increasing from the top to the bottom frame. (b) Plot of intensity of a second electrical point stimulus (S2) delivered at some time interval (abscissa) after a first stimulus (S1) that generates a plane wave. S2 fails to generate an excitation below the strength interval curve (solid red line). Above this curve, S2 only induces reentry inside the vulnerable window and a benign ectopic wave outside this window. (c) Schematic diagram illustrating the initiation of anatomical reentry by unidirectional block of propagation around an obstacle such as nonexcitable scar tissue. Unidirectional block requires spatial dispersion of refractoriness, which is represented by a longer refractory period in the brown region of tissue, and proper timing of the S2 stimulus for this region to recover its excitability after the time delay of propagation around the obstacle.

the boundaries. If it is delivered too soon, when the tissue is still in a refractory state that is not excitable, it has no effect. However, if it is delivered at an intermediate time that falls inside the

vulnerable window of **Figure 3b**, propagation of the circular depolarization wave is blocked rightward when it encounters refractory tissue, but not leftward where the tissue has had more time to recover its excitability after the passage of the first wave. The two intersections of the circular depolarization wavefront and the straight back of the plane wave from the S1 stimulus, which separates refractory and excitable regions, are the critical points where phase singularities are formed ($\oint \vec{\nabla} \theta \cdot \vec{d}l = \pm 2\pi$ around those points). The two resulting reentrant circuits around each singularity form a figure of eight.

Importantly, the radius of the circular region initially depolarized by the S2 stimulus sets the initial distance d between phase singularities. A larger stimulus intensity corresponds to injection of a larger current in the tissue and hence a larger depolarized region. As a result, if the stimulus intensity is lower than some threshold corresponding to the lower limit of the vulnerable window, the distance d between phase singularities is too short and spiral waves annihilate immediately or after a few rotations. In contrast, above this threshold, phase singularities are sufficiently far apart to prevent annihilation, and spirals survive, as in the example of **Figure 3a**. Above the upper limit of the vulnerable window, singularities no longer form because the size of tissue initially depolarized is too large. Experiments have largely validated this mechanism (46, 47) of initiation of reentry and further demonstrated that different conduction anisotropy in intracellular and extracellular spaces (bidomain effects) can lead to the formation of four phase singularities and quatrefoil reentry (two figure-of-eight reentrant circuits) (48, 49). Computer simulations have also yielded insights into dynamical wave properties influencing the vulnerable window (50).

In normal cardiac tissue, the stimulus intensity required to create a pair of phase singularities is orders of magnitude larger than the excitation threshold (minimum stimulus intensity) required to propagate a wave (**Figure 3b**). Therefore, a healthy heart is highly protected, whereas a diseased heart is susceptible to reentrant arrhythmias. The classic explanation for this difference is that reentry initiation is greatly facilitated if an excitation wave propagates into an arrhythmogenic tissue substrate where the refractory period is spatially heterogeneous, a property known as dispersion of refractoriness. **Figure 3c** illustrates how this property induces anatomical reentry around a permanently nonexcitable triangular-shaped obstacle, which splits the conduction path into left and right branches that connect below the obstacle. Only a low-intensity suprathreshold stimulus is required to initiate reentry when the refractory period is longer in a tissue patch on the right branch. In this case, downward propagation is blocked but proceeds through the left branch around the obstacle. Depending on timing, the wavefront can either be blocked again when it encounters this patch, or propagate through it if the tissue has had sufficient time to recover its excitability, thereby creating a reentrant circuit around the obstacle.

Even though the unidirectional block mechanism is illustrated here for anatomical reentry, dispersion of refractoriness also facilitates the initiation of functional reentry without obstacles. Hence, dispersion of refractoriness pushes downward the vulnerable window (**Figure 3b**) in a range where low-intensity electrical stimuli produced by tissue abnormalities can initiate reentry.

3. PRECURSOR ARRHYTHMOGENIC PATTERNS

3.1. Tissue-Scale Patterns: Spatially Discordant Alternans

Although static dispersion of refractoriness already exists in a healthy heart, it is not sufficient to initiate reentry. A long list of factors can enhance static dispersion in a diseased heart such as insufficient blood flow to a region (ischemia), excess fibrous tissue (fibrosis), tissue injury, or ionic

current changes (electrical remodeling). Although those factors are important, studies during the past decade have highlighted other factors that enhance dispersion of refractoriness dynamically, as opposed to statically. A paced (periodically stimulated) cardiac myocyte at normal heart rate typically exhibits period-1 dynamics with the same action potential duration (APD) at every beat. However, when paced sufficiently rapidly or under pathological conditions, a cell often exhibits period-2 dynamics characterized by an alternating sequence of long-short-long-short...APD known as repolarization alternans. An important discovery was made by David Rosenbaum and coworkers (51) who used optical mapping to image the spatial distribution of the phase and amplitude of those period-doubling oscillations of transmembrane voltage at the surface of a guinea pig's heart. Their key finding was that the phase of those period-doubling oscillations could reverse nonuniformly in space above a threshold pacing frequency, thereby leading to a state with two out-of-phase regions known as spatially discordant alternans (SDA). Furthermore, they demonstrated that such a pattern could create sufficient spatiotemporal dispersion of the refractory period to initiate reentry and VF.

This pattern of SDA is illustrated in **Figure 4a**, which shows a spatial map of alternans amplitude (difference of APD at two subsequent beats) from such an experiment. The top blue region alternates with a long-short-long APD sequence, while the bottom region alternates with a short-long-short sequence. The two regions are separated by a nodal line where the alternans amplitude vanishes. SDA is arrhythmogenic because on any given beat the APD, which primarily fixes the absolute refractory period, is different in blue and red regions, thereby creating or enhancing pre-existent dispersion of refractoriness. The discovery of SDA was important in the context of earlier clinical findings that patients whose ECG exhibit beat-to-beat changes of the T-wave (corresponding to ventricular repolarization) were at a higher risk of sudden cardiac death. Therefore the observation of SDA established a causal link between alternans at the single-cell and tissue levels, and increased risk of sudden death. For this reason, SDA has been widely investigated during the past decade through experimental studies in ventricular tissue (51–55) and tissue cultures (56–58), ionic model simulations of V_m (59–63) and coupled V_m - Ca_i (64–67) dynamics, and analytical approaches (62, 63, 67, 68).

3.2. Iterative Maps of Beat-to-Beat Dynamics

In the year following the discovery of SDA, two computational studies of ionic models showed that SDA can form spontaneously when cardiac tissue is paced from a point electrode and proposed qualitative explanations for this phenomenon (59, 60). One study also revealed that SDA forms generically as a periodic pattern in spatially extended tissue (60), which consists of an array of discordant regions with an intrinsic scale $\sim \lambda$ (**Figure 4b**).

Understanding how this pattern forms and what determines its scale is not practically feasible if one starts directly from the fundamental nonlinear wave Equation 1 of cardiac impulse. The difficulty to analyze the dynamical solution of this equation is manifest in the space-time plot of simulated transmembrane voltage $V_m(x, t)$ along a heart cable (top plot of **Figure 4b**). This plot shows that the cardiac AP propagates with a sharp depolarization wavefront moving at almost constant velocity, but a strongly oscillating repolarization waveback. This complex spatiotemporal pattern produced by a wave train instability can be reduced to a simpler pattern, which repeats every two beats, if one plots the APD at subsequent beats along the cable with the same coordinate x (plot below the space-time plot in **Figure 4b**). This suggests that a mathematical model that uses APD versus beat number as the basic dynamical variable instead of V_m would be more tractable to analyze SDA.

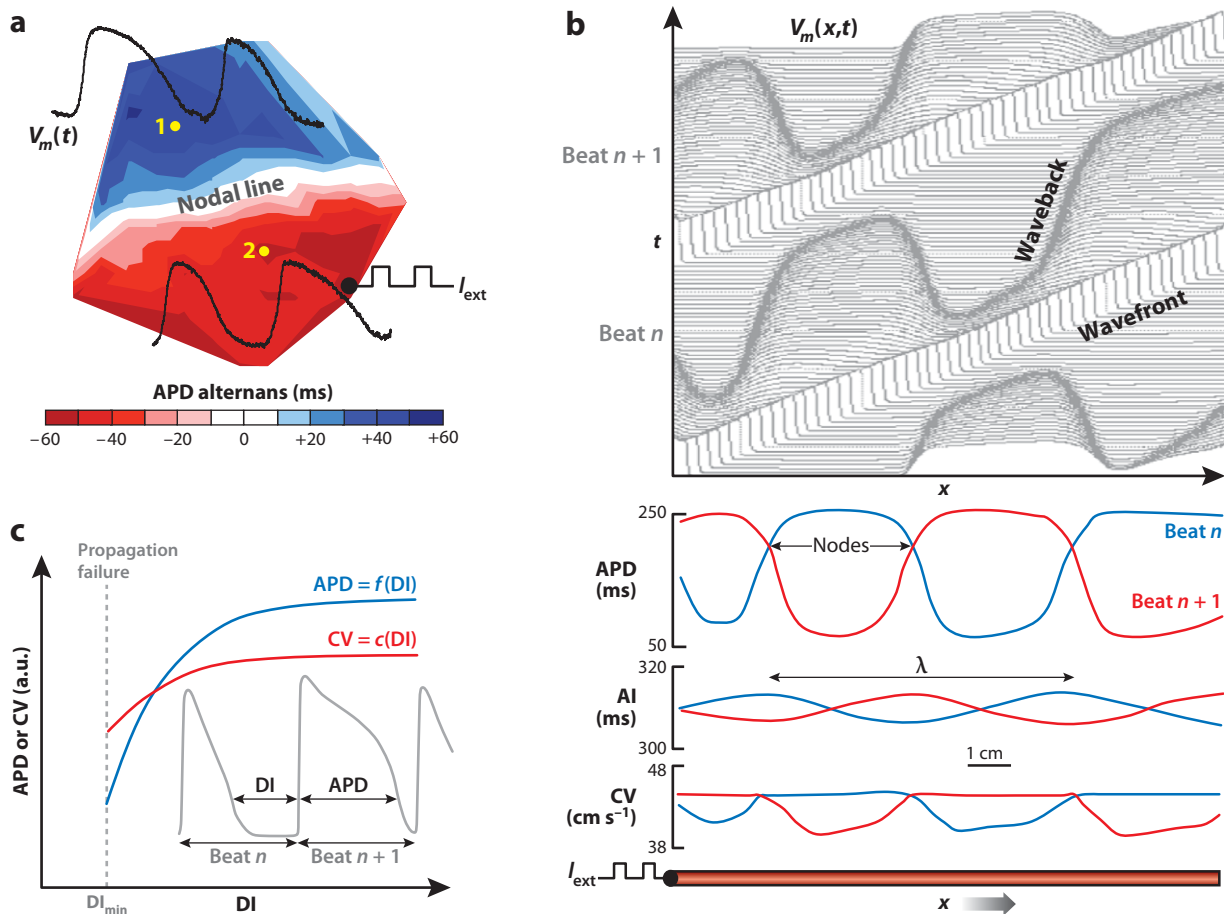


Figure 4

Experimental and computational examples of spatially discordant alternans and schematic representation of electrical restitution properties. (a) Spatial map of action potential duration (APD) alternans amplitude (difference of APD at two subsequent beats) at the surface of a guinea pig heart and transmembrane voltage V_m recordings at two points showing spatially out-of-phase alternans separated by a nodal line, which is a generic line defect of period-1 dynamics in period-2 excitable media (courtesy of David Rosenbaum). (b) Results of computer simulation of a 1D cardiac cable (60) periodically paced at its left end showing a space-time plot of $V_m(x, t)$ (vertically stacked plots of V_m versus x at short equal intervals of time) and corresponding spatial maps of APD, activation interval (AI), and conduction velocity (CV). (c) Schematic representation of APD- and CV-restitution curves that are the functional dependencies of APD and CV on the preceding diastolic interval (DI) between two waves.

Such a model can indeed be constructed based on two constitutive relations of cardiac tissue depicted in Figure 4c. The first is the APD-restitution relation between the APD and the preceding diastolic interval (DI), which is the time interval between two waves during which the ventricles relax to fill with blood. In computer simulations or experiments, the APD and DI can be conveniently defined as the time intervals that V_m spends above and below some arbitrary threshold close to the resting state (e.g., the value of V_m at 90% repolarization), respectively. The second is the relation between the wavefront speed and the preceding DI. This property is known as conduction velocity (CV) restitution, CV being synonymous with wavefront speed in cardiology.

The APD-restitution relation can be used to formulate an iterative map that describes beat-to-beat changes of APD. Such a map was first formulated graphically by cardiologists (69), independently formulated mathematically (70), and then widely used and extended to model V_m (e.g., 71–74) and V_m - Ca_i (75, 76) nonlinear dynamics (for reviews, see References 77–80).

Labeling by A_n and D_n the APD and DI that occur between two depolarizations, respectively, and by $T_n = A_n + D_n$ the activation interval (AI) between subsequent depolarizations, the APD-restitution relation yields the iterative map $A_{n+1} = f(D_n) = f(T_n - A_n)$. For an isolated cell paced at constant interval $T_n = \tau$, the map reduces to $A_n = f(\tau - A_n)$, which undergoes a period-doubling bifurcation to alternans when the slope $S \equiv f'(A^*)$ at the fixed point A^* [defined by $A^* = f(\tau - A^*)$] exceeds unity. To see this, substitute $A_n = A^* + \Delta_n$ into the map, which yields after linearization $\Delta_{n+1} \approx -S\Delta_n$, and hence $\Delta_n \approx \Delta_0(-1)^n S^n$. Therefore, perturbations grow exponentially in magnitude with alternating sign (APD alternans) for $S > 1$.

In a cable, the same map describes the local dynamics, but the AI, i.e., the time interval between two successive depolarizations, becomes spatially varying due to CV restitution (Figure 4b), which causes the wavefront speed and hence the arrival time of a wavefront at position x to vary along the cable from beat to beat (81). A wavefront activating the n^{th} action potential at position x along the cable takes a time $\Delta t_n(x) = \int_0^x dx'/c(D_{n-1}(x'))$ to travel from the paced end at $x = 0$ to x , where we denote by $c(DI)$ the CV-restitution curve. Hence, the time interval between subsequent activations (i.e. the AI) at x is $T_n(x) = \tau + \Delta t_{n+1}(x) - \Delta t_n(x)$, where $T_n(0) = \tau$ is the AI imposed by periodic pacing at $x = 0$, which gives

$$T_n(x) = \tau + \int_0^x \frac{dx'}{c(D_n(x'))} - \int_0^x \frac{dx'}{c(D_{n-1}(x'))}. \quad 3.$$

In addition to varying arrival times, electrical coupling between cells (Figures 1c,d) causes V_m and hence the APD at x to be influenced by nearby regions within a diffusion length $\xi \sim \sqrt{D_V A^*}$, where D_V is the voltage diffusion constant in Equation 1. This effect leads to a nonlocal spatial coupling of the iterative maps of the beat-to-beat dynamics:

$$A_{n+1}(x) = \int_0^L dx' G(x, x') f(T_n(x') - A_n(x')), \quad 4.$$

where the Kernel $G(x, x')$ captures the cumulative effect of voltage diffusion during one beat. The no-flux (zero current flow) boundary conditions ($\partial_x V_m = 0$) at the two ends of a cable of length L imply that $G(x, x') = G(x - x') + G(x + x') + G(2L - x - x')$, where the form

$$G(x) = \frac{1}{\sqrt{2\pi\xi^2}} e^{-\frac{x^2}{2\xi^2}} \left[1 + \frac{wx}{\xi^2} \left(1 - \frac{x^2}{\xi^2} \right) \right] \quad 5.$$

can be derived by inverting the cable equation (Equation 1) using the time-dependent Green's function for the diffusion equation (63). The Kernel is essentially a Gaussian on the scale of the diffusion length ξ , as physically expected, albeit with a slight asymmetry. This asymmetry reflects the fact that waves travel rightward such that cable regions to the left ($x' - x < 0$) depolarize sooner than regions to the right ($x' - x > 0$) of a cell at position x , thereby exerting different influences on that cell. Because the wavefront speed is large, this asymmetry is small. This Kernel identifies two key length scales: the diffusive length $\xi = \sqrt{2D_V A^*}$ and an additional length $w = 2D_V/c$ related to the Kernel asymmetry, where c is evaluated at the fixed point DI of the map $D^* = \tau - f(D^*)$.

3.3. Ginzburg-Landau Theory, Spontaneous Symmetry Breaking, and Length Scales

The set of Equations 3 and 4 together with the relation $T_n(x) = A_n(x) + D_n(x)$ completely specify the beat-to-beat dynamics. A numerical solution of those equations yields an SDA pattern almost identical to the one obtained from ionic model simulation (**Figure 4b**). Starting from those equations, it now becomes possible to obtain analytical insights into SDA formation by carrying out a weakly nonlinear multiscale analysis of those equations close to the period-doubling bifurcation (62, 63). This is done by expanding the APD in the form $A_n(x) \approx A^* + (-1)^n a(x, t) + \dots$ (and similarly $T_n \approx \tau + (-1)^n b(x, t) + \dots$). This expansion factors out the rapid beat-to-beat variation of period-doubling oscillations [through the $(-1)^n$ term], thereby extracting the slow dynamics of the alternans amplitude $a(x, t)$ close to the bifurcation on a continuous time $t = n\tau$. It yields the equation of the Ginzburg-Landau form

$$\tau \frac{\partial a}{\partial t} = \sigma a - ga^3 + \xi^2 \frac{\partial^2 a}{\partial x^2} - w \frac{\partial a}{\partial x} - \frac{1}{\Lambda} \int_0^x dx' a(x'), \quad 6.$$

where $\sigma = f''(\tau - \tau_c)/2$ measures the distance from the period-doubling bifurcation at $\tau = \tau_c$, with $\sigma > 0$ for $\tau < \tau_c$, $g = (f'')^2/4 - f'''/6$ is the Landau coefficient where prime superscripts denote higher-order derivatives of f at the fixed point, $\Lambda = c^2/(2c')$, where c' is the CV-restitution slope at the fixed point, and $\xi = \sqrt{2D_V A^*}$ and $w = 2D_V/c$ as before.

The amplitude equation (Equation 6) provides two important insights. First, it sheds light on the mechanism of formation of SDA from the fundamental viewpoint of symmetry breaking, thereby highlighting interesting similarities to phase transitions and nonequilibrium pattern formation. Second, it permits one to predict the scale of this pattern in terms of basic length scales ξ , w , and Λ , which can be themselves related to experimentally measurable properties of cardiac tissue.

Equation 6 without the last two terms on its right-hand-side (r.h.s.) is the standard time-dependent Ginzburg-Landau (TDGL) model of a one-dimensional Ising ferromagnet below the Curie temperature (for $\sigma > 0$), where the alternans amplitude $a(x, t)$ has a role analogous to the coarse-grained magnetization in this analogy. This stems from the fact that the phase of period-doubling oscillations is degenerate by π and hence the alternans amplitude has the same up-down symmetry as the Ising magnetization. However, the TDGL model does not produce an ordered pattern of up and down magnetic domains with an intrinsic wavelength, as exhibited by SDA (**Figure 4b**).

The interesting new physics comes from the last two terms on the r.h.s. of Equation 6. In particular, the last nonlocal (and also nonvariational) integral term produces a pattern-forming instability by amplifying small perturbations of the spatially homogeneous state $a = 0$ (corresponding to a periodic wave train without alternans). Although Equation 6 is invariant under the symmetry transformation $a \rightarrow -a$, the term $\int_0^x dx' a(x')/\Lambda$ breaks this symmetry locally at x , thereby acting locally as a magnetic field h . To see this, rewrite the local dynamics of Equation 6 in the variational form $\tau \dot{a} = -dV/da$, where $V(a) = -\sigma a^2/2 + ga^4/4 + ha$ and $h \equiv \int_0^x dx' a(x')/\Lambda$. At the pacing site, where $h = 0$, the double well potential $V(a)$ has two minima $a = \pm(\sigma/g)^{1/2}$ corresponding to the two phases of period-doubling oscillations. Starting in a cable where alternans are initially concordant, $a(x, t) > 0$, h will grow in magnitude away from the pacing site, thereby causing a to switch sign when h exceeds a threshold value where $V(a)$ loses its positive a minimum (analogous to a spinodal point). In the alternans setting, domain switching is equivalent to reversing the phase of alternans, thereby forming a discordant region. Because h grows in amplitude in x , phase reversal is predicted to occur first at the distal end of the cable, as observed in ionic model simulations and experiments. This unusual nonlocality originates here

from the fact that SDA is due to an instability of a plane wave train as opposed to an instability of an underlying spatially homogeneous state, as in other generic pattern-forming systems [such as Rayleigh-Bénard convection, Taylor-Couette flow, etc. (82)]. Hence, because a measures the amplitude of a secondary wave modulation of a primary wave train in a stationary laboratory frame ($a \sim$ the difference between the blue and red curves showing APD versus x at even and odd beats, respectively, in **Figure 4b**), the equation governing the spatiotemporal evolution of a (Equation 6) need not be local in space. **Figure 4b** illustrates a strongly nonlinear regime of SDA formation, whereas Equation 6 is strictly valid in a weakly nonlinear regime where a is nearly sinusoidal. However, simulations show that the more strongly nonlinear regime does not behave qualitatively differently than the weakly nonlinear regime, such that Equation 6 already suffices to capture salient features of SDA formation.

The above qualitative discussion of domain switching explains SDA formation but does not predict the pattern scale, which is also set by diffusive coupling. This scale can be predicted by a linear stability analysis of Equation 6 [i.e., substituting $a \sim \exp(ikx + \omega(k)t)$ to obtain an eigenvalue equation for ω_k]. This analysis (62, 63) predicts that patterns of SDA form spontaneously as standing or traveling waves with characteristic wavelength

$$\lambda = \begin{cases} 2\pi(\omega\Lambda)^{1/2} & \text{(standing),} \\ (4\pi/\sqrt{3})(\xi^2\Lambda)^{1/3} & \text{(traveling),} \end{cases} \quad 7.$$

with traveling waves being more unstable when the slope of the CV-restitution curve is sufficiently steep. **Figures 4a,b** illustrate standing wave patterns. Traveling patterns are similar but exhibit nodes (nodal lines) moving toward the pacing site and classical features of a convective instability (63). Although discussed in the context of V_m dynamics, the above prediction of λ also holds when Ca_i dynamics is included under the condition of positive Ca_i -to- V_m coupling (defined in the next section) owing to the universal character of the dynamics close to the bifurcation (67). Further from the bifurcation, this coupling brings in new interesting effects such as unidirectional pinning of SDA nodes (67).

For typical parameters of cardiac tissue, $D_V \sim 1 \text{ cm}^2/\text{s}$, $A^* \sim 0.2 \text{ s}$, and $c \sim 50 \text{ cm/s}$. This yields estimates of $\omega = 2D_V/c$ of a few hundred microns and $\xi = \sqrt{2D_V A^*}$ of a few mm. In contrast, $\Lambda = c^2/(2c')$ can be several orders of magnitude larger, varying between a few centimeters for traveling waves to several tens of centimeters for standing waves depending on the slope c' of the CV-restitution curve. The geometric means of those disparate length scales (Equation 7) is a pattern wavelength of a few centimeters, as observed. Accurate values of ω , ξ , and Λ can be extracted from ionic model simulations and can validate quantitatively the predictions of Equation 7 (62, 63). Characterizing those intrinsic length scales is more challenging in experiment where static heterogeneities are also present and tissue sizes are typically a fraction of λ , allowing only one nodal line (e.g., **Figure 4a**) or a few lines to form. However, experimental observations indeed reveal that nodes are generally dynamic entities, which can be induced to move inward toward the pacing site with increasing pacing frequency (52–55). Those observations support the basic theoretical picture that a symmetry-breaking pattern-forming instability is the mechanism of SDA in paced cardiac tissue.

Theoretical studies also support other initiation mechanisms of SDA, such as local phase reversal by an ectopic wave, which transforms spatially concordant into discordant alternans (60, 61). This alternate scenario is potentially important given that it links triggered beats to both an arrhythmogenic substrate and the initiation of reentry. In addition, the dynamics of SDA remains largely unexplored in the more complex setting where reentry has been initiated. A recent computational and theoretical study predicts that the number of nodal lines, which is topologically

constrained to be an odd number, should be 3 for spiral waves and 1 for anatomical reentry around a small obstacle (83). However, experimental tests of those predictions are lacking.

3.4. Voltage-Calcium Coupling and Subcellular Turing Patterns

During a normal contraction, intracellular Ca_i dynamics is essentially slaved to V_m . However, under pathological conditions, the intracellular Ca_i dynamics can become destabilized leading to period-doubling oscillations of Ca_i , known as Ca transient (CaT) alternans. Those CaT alternans can drive APD alternans through the effect of Ca_i on membrane currents and hence have an important arrhythmogenic role on a tissue scale. This has motivated both experimental (84–89) and theoretical studies (33–36) to elucidate their cellular origin. An unexpected experimental observation is that CaT alternans can become spatially discordant inside a heart cell (Figure 5), with two halves of the cell alternating out of phase (85, 88, 90–92). Explaining the role of spontaneous symmetry breaking in the emergence of this pattern requires a brief excursion in the cardiac biology of excitation-contraction coupling (31, 32).

A ventricular cell is organized as a row of contractile units known as sarcomeres (Figure 5a) comprised between T-tubules. T-tubules are invaginations of the outer membrane of the cell that permit LCC channels to penetrate deep into the cell, and they colocalize with Ca^{2+} release RyR channels at a large number (20,000 to 50,000) of dyadic junctions. RyR channels are embedded in the membrane of the sarcoplasmic reticulum (SR), a tubular connected network within each sarcomere that stores Ca^{2+} at high concentration (mM as opposed to μ M in the cytosol). Ca entry into the cell through L-type Ca channels induces RyR channels to open and release Ca (see Reference 94 for a first-passage time stochastic description of this local process). Ca is then pumped back into the SR to be available for release at the next beat. Furthermore, the CaT has two opposite effects on two Ca-sensitive membrane currents $I_{Ca,L}$ and I_{NCX} . A larger Ca release tends to inactivate L-type Ca channels and decrease $I_{Ca,L}$ (green arrow in Figure 5a) but increase I_{NCX} that extrudes one Ca^{2+} ion from the cell for every $3Na^+$ ion it brings in (red arrow). Depending on which of these two currents dominate, a larger CaT will either increase or decrease the APD, an effect described as positive or negative Ca_i -to- V_m coupling, respectively (75).

Figure 5b shows the result of a computational study of spatially distributed Ca dynamics that incorporates those basic ingredients of excitation-contraction coupling (95). This study reveals that CaT alternans can develop spatially concordantly or discordantly depending on the sign of the Ca_i -to- V_m coupling. For positive coupling (I_{NCX} predominance), CaT alternans develop spatially concordantly (top panel of Figure 5b), whereas for negative coupling ($I_{Ca,L}$ predominance), they develop spatially discordantly (bottom panel). Those different behaviors can be theoretically understood in terms of a Turing instability mechanism mediated by voltage and calcium diffusion (95). Starting from iterative maps describing beat-to-beat changes of APD and CaT amplitude, one can derive (similarly to Equation 6) the set of equations

$$\frac{da}{dt} = \alpha a + \frac{\beta}{\ell} \int_0^\ell dx c(x, t) \text{ and} \quad 8.$$

$$\frac{\partial c}{\partial t} = \delta c + \gamma a + \frac{\mu}{\ell} \int_0^\ell dx c(x, t) - \chi c^3 + D_c \frac{\partial^2 c}{\partial x^2}, \quad 9.$$

where a is the APD alternans amplitude ($A_n \approx A^* + (-1)^n a$), which is now spatially uniform on a cellular scale owing to the fast diffusion of voltage; c is the spatiotemporally varying CaT amplitude, $c_n(x) \approx c^* + (-1)^n c(x, t)$, where $c_n(x)$ denotes the peak Ca_i concentration during beat n at position $0 \leq x \leq \ell$ (ℓ = cell length); and $t = n\tau$, where τ is the pacing period. The coefficients in

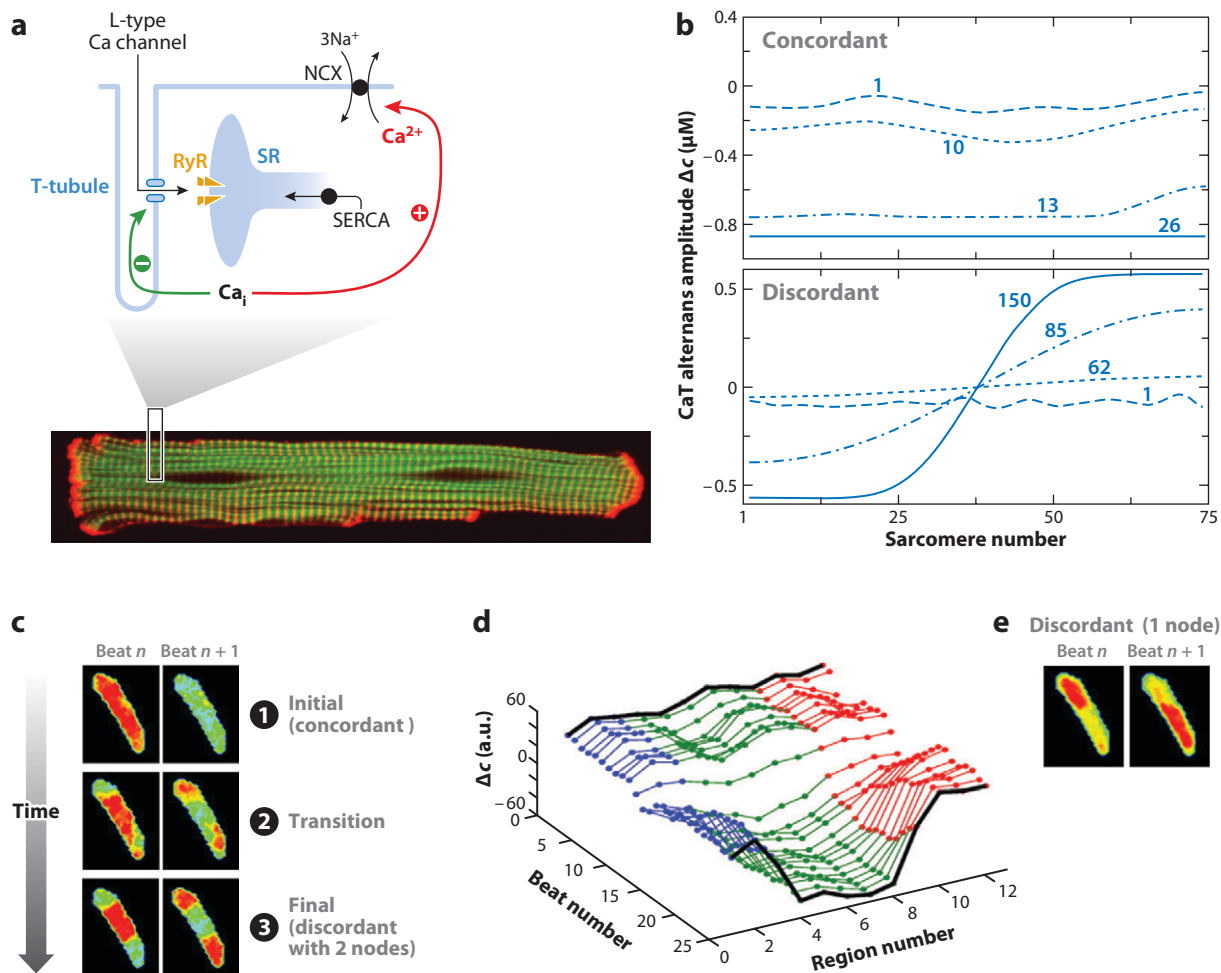


Figure 5

Voltage-calcium coupling and subcellular Turing patterns. (a) Experimental example of adult rat cardiac myocyte with sarcomeric actin labeled in green and sarcomeric alpha-actinin corresponding to Z-lines labeled in red (93). Contractile units (sarcomeres) are comprised between Z-lines. The top panel shows a magnified portion of one T-tubule at a Z-line and cardiac proteins underlying excitation-contraction coupling, including the Ryanodine receptor Ca^{2+} release channels (RyR), SERCA, which pumps Ca^{2+} ions into the sarcoplasmic reticulum (SR), and the sodium-calcium exchanger NCX, which exchanges one Ca^{2+} ion for three Na^+ ions across the sarcolemmal membrane. As in Figure 2b, Ca_i denotes the cytosolic Ca concentration. (b) Results of computer simulations of subcellular Ca dynamics (95) showing the spatial distribution of the Ca transient (CaT) alternans amplitude as a function of position (sarcomere #) along the cell's main axis at different beat numbers. CaT alternans develop spatially concordantly (top) and discordantly (bottom) for positive (top) and negative (bottom) Ca_i -to- V_m coupling, respectively. (c-e) Result of an experiment (92) where the voltage and subcellular Ca activity are simultaneously recorded in a paced isolated cardiac myocyte. Spatially concordant CaT alternans are induced to become spatially discordant by the use of an electrical feedback scheme that switches the sign of Ca_i -to- V_m coupling from positive to negative. (c) Fluorescence image of Ca_i concentration inside the cell during (1) initially concordant alternans, (2) the transition to discordant alternans, and (3) steady-state discordant alternans with two nodes. (d) Space-time plot of CaT amplitude versus beat number and region number along the cell axis (where each region includes a few sarcomeres) after control is switched on. (e) Same as bottom image in panel c for a different control experiment in the same cell showing formation of a discordant alternans pattern with a single node.

Greek letters can all be related to elements of the Jacobian of the iterative maps of the local dynamics linearized around the period-1 fixed point (95). In addition, D_c is proportional to the intracellular diffusivity of Ca^{2+} ions.

In the classic Turing mechanism of instability, patterns form spontaneously through the interaction of a slow diffusing activator and a fast diffusing inhibitor. Even though the details of Equations 8 and 9 differ from those analyzed by Turing (96) [also Gierer & Meinhardt (97)], the same type of interaction between Ca and voltage arises when (i) CaT alternans are due primarily to an instability of Ca cycling ($\delta > 0$ and $\alpha < 0$), in which case c can both auto-catalyze itself and produce a , and (ii) the Ca_T -to- V_m coupling is negative, in which case APD alternans inhibit CaT alternans (i.e., a inhibits c). Those two conditions and the slow diffusion of Ca^{2+} ions ($D_c/D_V \sim 10^{-6}$) create the setting for short-range activation and long-range inhibition. A linear stability carried out by substituting a and $c \sim \exp(ikx + \omega t)$ into Equations 8 and 9 predicts that spatially discordant patterns will form when $\beta\gamma < 0$ and $\delta + \mu - \alpha > 0$, which is the condition for the Ca_T -to- V_m coupling to be negative (95).

An experimental test of this Turing mechanism was recently performed in a ventricular cell, where Ca_T was imaged with a Ca dye at the same time that V_m was recorded (92). Because Ca_T -to- V_m coupling is often positive, this experimental study made clever use of a feedback control scheme that alters the pacing interval based on APD changes from previous beats (Section 5.1). In the setting of an isolated cell, this scheme can be shown theoretically to have an effect analogous to switching the Ca_T -to- V_m coupling from positive to negative (98). **Figure 5c–e** illustrates one of those experiments where switching on feedback control has the anticipated effect of suppressing APD alternans and inducing a symmetry-breaking instability that produces spatially discordant CaT alternans. This pattern is a rather unique biological example where a Turing instability mechanism can be so clearly demonstrated and controlled, and the long-range inhibitor is an electrical as opposed to a chemical signal.

As for tissue-scale discordant alternans, subcellular CaT alternans can become discordant by other mechanisms. In particular, subcellular Ca dynamics exhibits excitable properties and supports Ca^{2+} waves that can be spontaneously initiated in situations of Ca overload, where the SR Ca concentration is larger than normal. Those spontaneous Ca waves can then reverse the phase of CaT alternans, as experimentally observed (91), in a way similar to an ectopic wave on a tissue scale. CaT alternans that are discordant on a subcellular scale produce no APD alternans. However, a nonlinear analysis of Equations 8 and 9 shows that spatially concordant and discordant subcellular patterns generally coexist for negative coupling away from onset of instability (35). This bistability makes the pattern selection history-dependent on both subcellular (35) and tissue scales (64, 66). Moreover, concordant patterns generate out-of-phase cellular APD and CaT alternans, which are indeed observed under conditions of negative Ca_T -to- V_m coupling ($I_{Ca,L}$ predominance) (89). In addition, the stochastic nature of Ca release can strongly influence the subcellular Ca dynamics and lead to phase reversal even without Ca^{2+} waves (35). Those dynamical factors together with observed cell-to-cell heterogeneities (88) make it challenging to bridge subcellular and tissue-scale phenomena in the setting of Ca-mediated alternans.

4. WAVE TURBULENCE

4.1. Mother Rotor and Wandering Wavelets

Once the tissue substrate becomes sufficiently disordered, trigger-substrate interactions can initiate reentry that generally degenerates into VF (**Figure 1**). The wave turbulence associated with VF has been extensively studied both experimentally (9–17) and computationally (99–107). Those studies have contrasted two differing mechanisms. The first assumes that a single stable reentrant

circuit (a mother rotor) that is long-lived in some region of the heart drives VF (12–14). In this interpretation, wavebreaks typically observed at the surface of the heart are the result of static dispersion of refractoriness. Wavebreaks occur at regions of prolonged refractoriness that cannot keep up with the mother rotor frequency, but are not the driver of VF. An opposite view postulates that wavebreaks, produced dynamically by spiral or scroll wave instabilities that would already be present in homogeneous tissue, are the main driver of VF (10, 11) and lead to multiple wavelets. This scenario has also been described as the restitution hypothesis following computer simulations linking steep APD restitution to spiral wave breakup in homogeneous 2D tissue (99, 100) and subsequent experiments supporting this link (10) and showing that flattening APD restitution can suppress VF (11).

Progress has been made during the past decade to reconcile these conflicting views by showing that different mechanisms of VF can operate under different conditions (15) and that drugs used to uncouple excitation and contraction for the purpose of optical mapping alter those mechanisms (16). The conclusion from those studies is that wavebreaks caused by wave instabilities are the main driver of VF for normal tissue with high excitability, whereas the mother rotor scenario may prevail for tissue with weaker excitability and shorter APD.

4.2. Spiral Wave and Filament Breakup

Independently of experiments, computer simulations have shown that both 2D and 3D wave instability mechanisms are capable of producing VF with multiple wavelets typically seen in optical surface maps (**Figure 1e**). Steep APD restitution can maintain wavebreaks in 2D (100–102) and 3D (106). In addition, vortex filaments can break up to produce 3D wave turbulence (108) for parameters where spiral wave breakup does not occur in 2D (103, 104) (**Figure 1f**). Filament breakup can occur when the filament tension is negative, which causes the filament to elongate and break up when it collides with tissue boundaries. Although filament tension is generically negative for weak excitability where it can be analytically predicted (see Reference 22 and earlier references therein), it is also negative for some parameters of high excitability (109). For positive tension, filament breakup is also possible due to the rotation of the fiber axis (horizontal axis in **Figure 2c**) across the ventricular wall. This rotation induces a twist that can destabilize scroll waves through sproing (110), a helical filament instability that resembles twist-induced instabilities of elastic rods. Theoretical progress has been made to characterize this instability in isotropic media (111–113), where twist is enforced through boundary conditions. There have also been theoretical attempts to incorporate the effect of fiber rotation (114, 115). However, twist-induced filament dynamics in 3D cardiac tissue is still poorly understood. A recent experiment where fiber rotation was enhanced in a transgenic animal model indicates that fiber twist may facilitate turbulence (116).

From all studies to date, a likely scenario is that APD restitution, twist-induced filament instabilities, and static heterogeneities jointly contribute to produce wavebreaks that maintain VF in normal tissue. It is also possible that, depending on initial conditions, different dynamical attractors produce different forms of VF in the same heart, as some simulations suggest (107).

4.3. Other Mechanisms

Other mechanisms of VF can also exist in settings where electrophysiological properties of the heart are altered. One example is the long QT (LQT) syndrome (characterized by a longer time interval between Q and T in the ECG; cf. **Figure 1b**) associated with ion channel mutations that reduce the magnitude of repolarizing currents (e.g., missing I_{Ks} in LQT1 or I_{Kr} in LQT2). This

reduction increases the duration of the plateau phase of the AP (**Figure 2a**) and hence the QT interval in the ECG. Spontaneous depolarizations occurring during this plateau phase, commonly known as early afterdepolarizations (38–41) can become focal sources of waves that both initiate and interact with reentrant circuits. Recent computational studies (117–119) have shed light on the complex dynamics of multiple foci. In addition, transgenic animal models that mimic the pathophysiology of the human LQT syndrome are creating a unique opportunity to investigate experimentally mechanisms of VF in this setting (120).

5. CONTROL OF PRECURSOR PATTERNS AND WAVE TURBULENCE

5.1. Feedback Control of Alternans

An attractive alternative to drug therapy is to use low-intensity stimuli to prevent instabilities that can initiate life-threatening reentrant arrhythmias. Several studies along this line have focused on the control of alternans (121–128). It has so far not been experimentally possible to suppress alternans completely uniformly in spatially extended tissue, for theoretical reasons (124) explained below. However, it has been possible to reduce their amplitude at an arbitrary desired location (126) along a one-dimensional heart cable. This was achieved by using a feedback scheme (121, 122, 125, 126) that continuously monitors the transmembrane potential at some arbitrary location x_r along the cable and then uses this information to modify the timing of pacing stimuli at the pacing site ($x = 0$). More specifically, this scheme computes the APD difference at two subsequent beats at the off-site $A_{n+1}(x_r) - A_n(x_r)$ and then modifies the pacing interval by an amount proportional to this difference:

$$T_{n+1}(0) = \tau + \frac{\gamma}{2}[A_{n+1}(x_r) - A_n(x_r)], \quad 10.$$

if $A_{n+1}(x_r) < A_n(x_r)$, or keeps the interval constant $T_{n+1}(0) = \tau$ if $A_{n+1}(x_r) > A_n(x_r)$, where $\gamma > 0$ is the feedback gain. The results of an experimental implementation of this scheme in a one-dimensional Purkinje fiber are shown in **Figure 6a**, which compares the spatial distribution of APD recorded from six electrodes along the cable at two subsequent beats for the case without control (top figure) and with control at three different locations (three plots below). Remarkably, in all cases, the feedback control scheme completely suppresses alternans at the off-site even though the pacing interval is modified only at the pacing site.

Those experimental findings can be analyzed in the theoretical framework laid out in Section 3.1. The above feedback control scheme adds a term $-\gamma a(x_r, t)/2$ to the r.h.s. of Equation 6 (124, 126). In a short cable where CV is approximately constant, linear eigenmodes of alternans of the form $a(x, t) = \Psi(x)e^{\Omega t}$ have a spatially varying part that obeys a forced Helmholtz equation:

$$\xi^2 \frac{d^2 \Psi(x)}{dx^2} + (\sigma - \Omega) \Psi(x) = \frac{\gamma}{2} \Psi(x_r), \quad 11.$$

which must be solved subject to the boundary condition $d\Psi(x)/dx = 0$ at the two cable ends ($x = 0$ and $x = L$). The elementary solution of this eigenvalue problem shows that the spatially uniform mode $\Psi_0 \sim \text{constant}$ has an eigenvalue $\Omega_0 = \sigma - \gamma/2$, which becomes negative for large enough γ . Thus, this mode, which is the one observed without control (top of **Figure 6a**) is suppressed by the feedback scheme. However, higher-order quantized modes with eigenvectors of the form

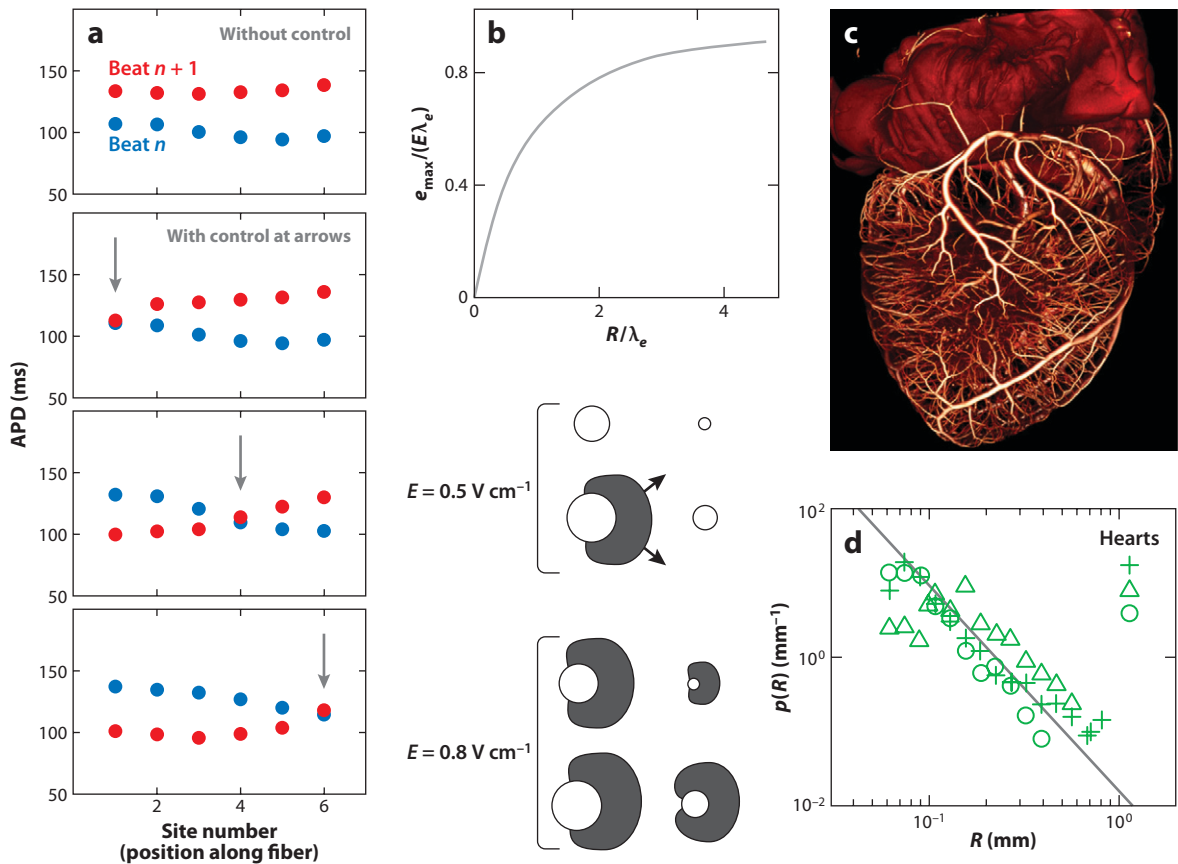


Figure 6

Control of arrhythmias. (a) Experimental results of off-site control of alternans in a 2-cm Purkinje fiber stimulated from the left end (126). APD distribution at beat n (blue) and beat $n + 1$ (red) showing spatially concordant alternans without control (top plot) and formation of a node at three positions of the control site (x_r) indicated by the gray arrows (bottom three plots). (b–d) Plots illustrating the mechanism of low-energy defibrillation by wave emission from cardiac tissue heterogeneities (130, 132). (b) Plot of $e_{\max}/(E\lambda_e)$ versus R/λ_e where e_{\max} is the maximum depolarized value of $V_m - V_{\text{rest}}$ induced by an electric field E at the perimeter of an obstacle of radius R , where λ_e is the electrotonic coupling length. The eight illustrations below panel b are results of computer simulations (130) for two E values, and the same four R values for each E , illustrating that a larger E is able to recruit smaller heterogeneities (130). (c) Micro-CT scan image of network structure of coronary arteries of different radii in ventricular muscle imaged by injection of a contrast agent (courtesy of Flavio Fenton). (d) An example of a probability distribution of different radii obeying a power law (132), where different symbols correspond to different hearts.

$$\Psi_n(x) \sim \cos \frac{n\pi x_r}{L} + \left(\frac{2n^2\pi^2\xi^2}{\gamma L^2} - 1 \right) \cos \frac{n\pi x}{L}, \quad (n \geq 1) \quad 12.$$

are unchanged by feedback control and have eigenvalues $\Omega_n = \sigma - (n\pi\xi/L)^2$. Therefore, the $n = 1$ mode with the largest Ω is the most unstable. Because the diffusive scale ξ is on a mm scale (Section 3.1) while $L \approx 2$ cm, and hence $x_r/L < 1$, it follows that $\Omega_1 \approx \sigma$, and $\Psi_1(x) \sim \cos(\pi x_r/L) - \cos(\pi x/L)$. Therefore, the alternans node occurs at $x = x_r$, which is precisely the experimentally observed mode for different off-site locations (Figure 6a). This explains experimental observations but also shows that complete suppression of alternans is generically not possible from

a single control site owing to the fundamental wave nature of alternans. More recent theoretical work suggests that extension of such schemes, which use multiple recording electrodes, could conceivably lead to further improvements (128).

5.2. Control of Wave Turbulence

If initiation of wave turbulence cannot be prevented, the most reliable method to restore the heart to a normal rhythm is defibrillation via a high-intensity electrical shock that is aimed at terminating all waves by exciting resting tissue regions to make them refractory. For patients with a high risk of occurrence of VF, the implantable cardioverter defibrillator is the most reliable way to prevent sudden cardiac death. Such a device first attempts to reset the heart to a normal rhythm through anti-tachycardia pacing (ATP), a sequence of low-amplitude stimuli, and then delivers a high-intensity shock if ATP fails. ATP may succeed to unpin vortices and control VT (129), but not generally VF with many vortices of different phases. Although defibrillation is generally effective in this case, high-intensity shocks can damage heart tissue and are painful, thereby seriously degrading the quality of life of some patients.

An idea recently pursued to reduce the intensity of electrical shocks is to exploit the emission of excitation waves from intrinsic heterogeneities of the heart of various sizes (130–133). The underlying physics of this effect can be theoretically understood by solving the 2D extension of the cable equation (Equation 1) in the presence of a uniform electric field $\vec{E} = E\hat{x}$ and a circular obstacle of radius R representing a heterogeneity in the heart. In the situation where the membrane potential is close to its resting value V_{rest} , the field $e(x, y) = V_m(x, y) - V_{\text{rest}}$ obeys the equation $\nabla^2 e - e/\lambda_e^2 = 0$, where λ_e is an electrotonic length of order mm. Solution of this equation, subject to the appropriate boundary condition at the perimeter of the obstacle and $e \rightarrow 0$ far from it, yields the solution in polar coordinate (130)

$$e(r, \theta) = -\frac{K_1(r/\lambda_e)}{K'_1(r/\lambda_e)} E \lambda_e \cos \theta. \quad 13.$$

Thus, e has its maximum value $e_{\text{max}} = -E\lambda_e(K_1(R/\lambda_e)/K'_1(R/\lambda_e))$ at $\theta = 0$ on the circle boundary, which will act as the focal source of an excitation wave when e_{max} exceeds the excitation threshold ($e_{\text{max}} > e_{\text{threshold}}$). A plot of $e_{\text{max}}/(E\lambda_e)$ versus R/λ_e (Figure 6b) shows that, for a fixed E , only heterogeneities with $R > R_{\text{min}}(E)$ will become wave sources where the scaling $R_{\text{min}}(E) \sim 1/E$ follows from the above solution. This implies that increasing E will generally increase the number of wave-emitting sources in cardiac tissue where heterogeneities of different sizes are present. Consequently, although a high-intensity shock will generally be necessary to trigger excitable waves from an extremely large number of heterogeneities down to very small sizes, smaller electric fields may already suffice to excite enough waves from larger obstacles near spiral wave cores to stop wave turbulence, thereby lowering the defibrillation threshold.

This low-energy approach to taming wave turbulence is supported by recent in vivo experimental studies in atrial (131, 133) and ventricular (132) tissue, which show that the defibrillation threshold can be significantly lowered by using a pulsed electric field based on the above principle. Moreover, one study (132) characterized multiscale heterogeneities in ventricular muscle by imaging the ramified network structure of coronary arteries (Figure 6c) and extracting from it a probability distribution of artery radius $p(R)$ (Figure 6d), found to obey an approximate scaling law $p(R) \sim R^\alpha$. This distribution, in turn, can be used to derive scaling laws for the density $\rho(E)$ of recruited wave-emitting sources and for the characteristic time $\tau(E)$ for tissue depolarization. For example, for the former, the expression $\rho(E) = (N_{\text{total}}/V) \int_{R_{\text{min}}(E)}^{R_{\text{max}}} p(R) dR$ follows from simply

assuming that heterogeneities are uniformly distributed in space. Those scaling laws provide a fundamental understanding of the response of cardiac tissue to an applied field in relation to extinguishing reentrant circuits. Practical implementation of those concepts holds promise for improving implantable devices to achieve reliable defibrillation with lower energy shocks.

6. SUMMARY AND OUTLOOK

The past decade has witnessed rapid progress in our basic understanding of complex dynamical phenomena underlying the initiation, maintenance, and control of life-threatening reentrant cardiac arrhythmias.

For initiation, the discovery of SDA has led to the recognition that dynamical instabilities can contribute to an arrhythmogenic tissue substrate by creating spatiotemporal (as opposed to only static) variations of the refractory period of cardiac tissue. Simulations and theory, in turn, have shown that this pattern forms via an instability that spontaneously breaks translational symmetry of the underlying state where the refractory period is spatially uniform, and produces a wavy modulation of this period on an intrinsic wavelength independent of tissue size. Furthermore, universal aspects of this pattern have been understood in a Ginzburg-Landau theoretical framework, which relates this wavelength to basic length scales characterizing diffusive coupling and CV restitution. Experiments, simulations, and theory have also highlighted the importance of the dynamical coupling between electrical excitation and intracellular Ca signaling, and the sign of this coupling. In particular, negative coupling leads to additional diffusive (Turing-type) instabilities on subcellular scales. It also promotes patterns of Ca and voltage alternans that are both strongly history-dependent and disordered on multiple scales between cell and tissue. Voltage-Ca coupling is also likely to play a key role in the formation triggers (early and delayed after depolarizations) that interact with an arrhythmogenic substrate to initiate reentry. However, this role remains to be better understood.

For maintenance, several mechanisms of wave turbulence have been postulated based on experimental observations and computer simulations. Although data to date support the view that turbulence in normal tissue is driven predominantly by wavebreaks, the nature of this turbulence is hard to infer from only surface optical maps of voltage or Ca activity. Experiments that image the activity below the surface with the spatiotemporal resolution necessary to track vortex filaments are necessary to make the comparisons of simulations and experiments less speculative, especially given the unknowns of electrophysiological parameters in computer models. Furthermore, how turbulence is initiated and maintained in the context of specific diseases linked to genetic mutations and heart failure remains to be understood both theoretically and experimentally.

Attempts to dynamically control the tissue substrate to prevent reentry have so far been only partially successful. Alternans can be reduced only at a control site by modifying the timing of pacing stimuli, but not uniformly. Therefore, novel schemes with multiple control sites are needed to improve outcomes. Attempts to directly control turbulence by exploiting wave-emitting properties of tissue heterogeneities appear more promising, and methods that use low-energy pulsed electric fields based on this concept could conceivably find their way into implantable defibrillators in the near future.

Beyond the topics reviewed in this article, there are important challenges that lie at the intersection of nonlinear dynamics, computational modeling, and systems biology. A major long-term goal is to develop drug and gene therapies that alter the function of one or several molecular components of the heart excitation-contraction system to reduce arrhythmogenicity. Recent work has highlighted two major difficulties in achieving this goal. First, biologically detailed

ionic models have become extremely complex and it is therefore generally difficult to uniquely determine their parameters from fits to experimental data (134–136). Reduced models circumvent this problem by describing emergent phenomena such as discordant alternans in terms of experimentally measurable constitutive properties (such as restitution, diffusive coupling, Ca-voltage coupling, etc.) but are not as directly linkable to molecular components. Second, cardiac electrophysiological parameters, and hence responses to therapies, may be highly variable due to genetic variations within the same population (137). The combination of a systems biology approach, computer modeling, and nonlinear dynamics offers a promising avenue to characterize this variability and examine its arrhythmogenic consequence, as a basis to improve molecular-based therapies.

DISCLOSURE STATEMENT

The author is not aware of any affiliations, memberships, funding, or financial holdings that might be perceived as affecting the objectivity of this review.

ACKNOWLEDGMENTS

Part of this work was supported by grants from the National Institutes of Health.

LITERATURE CITED

1. Winfree AT. 1972. *Science* 175:634–36
2. Winfree AT. 1973. *Science* 181:937–39
3. Winfree AT. 1987. *When Time Breaks Down*. Princeton, NJ: Princeton Univ. Press
4. Lechleiter J, Girard SE, Peralta EG, Clapham DE. 1991. *Science* 252:123–26
5. Foerster P, Muller SC, Hess B. 1990. *Development* 109:11–16
6. Lee KJ, Cox EC, Goldstein RE. 1996. *Phys. Rev. Lett.* 76:1174–77
7. Salama G, Choi BR. 2007. *J. Electrocardiol.* 40:S56–61
8. Cherry EM, Fenton FH. 2008. *New J. Phys.* 10:125016
9. Witkowski FX, Leon LJ, Penkoske PA, Giles WR, Spano ML, et al. 1998. *Nature* 392:78–82
10. Koller ML, Riccio ML, Gilmour RF. 1998. *Am. J. Physiol.* 275H:1635–42
11. Garfinkel A, Kim Y-H, Voroshilovsky O, Qu Z, Kil JR, et al. 2000. *Proc. Natl. Acad. Sci. USA* 97:6061–66
12. Jalife J. 2000. *Annu. Rev. Physiol.* 62:25–50
13. Zaitsev AV, Berenfeld O, Mironov SF, Jalife J, Pertsov AM. 2000. *Circ. Res.* 86:408–17
14. Samie FH, Berenfeld O, Anumonwo J, Mironov SF, Udassi S, et al. 2001. *Circ. Res.* 89:1216–23
15. Wu TJ, Lin SF, Weiss JN, Ting CT, Chen PS. 2002. *Circulation* 106:1859–66
16. Wu TJ, Lin SF, Baher A, Qu Z, Garfinkel A, et al. 2004. *Circulation* 110:2110–18
17. Nash MP, Mourad A, Clayton RH, Sutton PM, Bradley CP, et al. 2006. *Circulation* 114:536–42
18. Karma A. 1990. *Phys. Rev. Lett.* 65:2824–27
19. Winfree AT. 1991. *Chaos* 1:303–34
20. Barkley D. 1992. *Phys. Rev. Lett.* 68:2090–93
21. Barkley D. 1994. *Phys. Rev. Lett.* 72:164–167
22. Hakim V, Karma A. 1999. *Phys. Rev. E.* 60:5073–105
23. Noble D. 1962. *J. Physiol.* 160:317–52
24. Beeler GW, Reuter H. 1977. *J. Physiol.* 268:177–210
25. Luo CH, Rudy Y. 1991. *Circ. Res.* 68:1501–26
26. Hund TJ, Rudy Y. 2004. *Circulation* 110:3168–74
27. ten Tusscher KHWJ, Bernus O, Hren R, Panfilov AV. 2006. *Prog. Biophys. Mol. Biol.* 90:326–45
28. Mahajan A, Shiferaw Y, Sato D, Baher A, Olcese R, et al. 2008. *Biophys. J.* 94:392–410

29. Keener JP, Sneyd J. 2009. *Mathematical Physiology* (Interdisciplinary Applied Mathematics, Vol. 8). New York: Springer. 2nd ed.
30. Rudy Y. 2012. In *Comprehensive Biophysics*, Vol. 9: Simulation and Modeling, ed. EH Egelman, pp. 268–327. Oxford, UK: Academic
31. Bers DM. 2002. *Nature* 415:198–205
32. Bers DM. 2008. *Annu. Rev. Physiol.* 70:23–49
33. Shiferaw Y, Watanabe MA, Garfinkel A, Weiss JN, Karma A. 2003. *Biophys. J.* 85:3666–86
34. Restrepo JG, Weiss JN, Karma A. 2008. *Biophys. J.* 95:3767–89
35. Restrepo JG, Karma A. 2009. *Chaos* 19:037115
36. Rovetti R, Cui X, Garfinkel A, Weiss JN, Qu Z. 2010. *Circ. Res.* 106:1582–91
37. Gaur N, Rudy Y. 2011. *Biophys. J.* 100:2904–12
38. Tanskanen AJ, Greenstein JL, O'Rourke B, Winslow RL. 2005. *Biophys. J.* 88:85–95
39. Lerma C, Krogh-Madsen T, Guevara M, Glass L. 2007. *J. Stat. Phys.* 128:347–74
40. Sato D, Xie L-H, Nguyen TP, Weiss JN, Qu Z. 2010. *Biophys. J.* 99:765–73
41. Keener JP, Newby JM. 2011. *Phys. Rev. E.* 84:011918
42. Chen W, Aistrup GL, Wasserstrom JA, Shiferaw Y. 2001. *Am. J. Physiol. Heart Circ. Physiol.* 300: H1794–805
43. Chen W, Asfaw M, Shiferaw Y. 2012. *Biophys. J.* 102:461–71
44. Bueno-Orovio A, Cherry EM, Fenton FH. 2008. *J. Theor. Biol.* 253:544–60
45. Winfree AT. 1989. *J. Theor. Biol.* 138:353–405
46. Chen PS, Wolf PD, Dixon EG, Danieleley ND, Frazier DW, et al. 1988. *Circ. Res.* 62:1191–209
47. Frazier DW, Wolf PD, Wharton JM, Tang AS, Smith WM, Ideker RE. 1989. *J. Clin. Invest.* 83:1039–52
48. Roth BJ, Saypol JM. 1991. *Int. J. Bifurcat. Chaos* 1:927–92
49. Lin SF, Roth BJ, Wikswo JP Jr. 1999. *J. Cardiovasc. Electrophysiol.* 10:574–86
50. Yang MJ, Tran DX, Weiss JN, Garfinkel A, Qu Z. 2007. *Am. J. Physiol. Heart Circ. Physiol.* 293: H1781–90
51. Pastore JM, Girouard SD, Laurita KR, Akar FG, Rosenbaum DS. 1999. *Circulation* 99:1385–94
52. Fox JJ, Riccio ML, Hua F, Bodenschatz E, Gilmour RF Jr. 2002. *Circ. Res.* 90:289–96
53. Hayashi H, Shiferaw Y, Sato D, Nihei M, Lin S-F, et al. 2007. *Biophys. J.* 92:448–60
54. Mironov S, Jalife J, Tolkacheva EG. 2008. *Circulation* 118:17–25
55. Morales OZE, Song Y-K, Peng X, Odening KE, Buxton AE, et al. 2009. *J. Physiol.* 587:4661–80
56. Hwang S-M, Kim TY, Lee KJ. 2005. *Proc. Natl. Acad. Sci. USA* 102:10363–68
57. Bien H, Yin J, Entcheva E. 2006. *Biophys. J.* 90:2628–40
58. Jia Z, Bien H, Shiferaw Y, Entcheva E. 2012. *Biophys. J.* 102:1294–302
59. Qu Z, Garfinkel A, Chen PS, Weiss JN. 2000. *Circulation* 102:1664–70
60. Watanabe MA, Fenton FH, Evans SJ, Hastings HM, Karma A. 2001. *J. Cardiovasc. Electrophysiol.* 12: 196–206
61. Echebarria B, Karma A. 2007. *Eur. Phys. J.* ST146:217–31
62. Echebarria B, Karma A. 2002. *Phys. Rev. Lett.* 88:208101
63. Echebarria B, Karma A. 2007. *Phys. Rev. E.* 76:051911
64. Sato D, Shiferaw Y, Qu Z, Garfinkel A, Weiss JN, et al. 2006. *Circ. Res.* 99:520–27
65. Sato D, Shiferaw Y, Qu Z, Garfinkel A, Weiss JN, Karma A. 2006. *Biophys. J.* 92:L33–35
66. Zhao X. 2008. *Phys. Rev. E.* 78:11902
67. Skardal PS, Karma A, Restrepo JG. 2012. *Phys. Rev. Lett.* 108:108103
68. Dai S, Schaeffer DG. 2008. *SIAM J. Appl. Math.* 69:04719
69. Nolasco JB, Dahlen RW. 1968. *J. Appl. Physiol.* 25:191–96
70. Guevara MR, Ward G, Shrier A, Glass L. 1984. *IEEE Comput. Cardiol.* 1984:167–70
71. Chialvo DR, Gilmour RF, Jalife J. 1990. *Nature* 343:653–57
72. Fox JJ, Gilmour RF Jr, Bodenschatz E. 2002. *Phys. Rev. Lett.* 89:198101
73. Fox JJ, Bodenschatz E, Gilmour RF Jr. 2002. *Phys. Rev. Lett.* 89:138101
74. Berger CM, Zhao X, Schaeffer DG, Dobrovolny HM, Krassowska W, Gauthier DJ. 2007. *Phys. Rev. Lett.* 99:58101

75. Shiferaw Y, Sato D, Karma A. 2005. *Phys. Rev. E*. 71:021903
76. Qu Z, Shiferaw Y, Weiss JN. 2007. *Phys. Rev. E*. 75:011927
77. Shiferaw Y, Qu Z, Garfinkel A, Karma A, Weiss JN. 2006. *Ann. N. Y. Acad. Sci.* 1080:376–94
78. Weiss JN, Karma A, Shiferaw Y, Chen P-S, Garfinkel A, Qu Z. 2006. *Circ. Res.* 98:1244–53
79. Karma A, Gilmour RF. 2007. *Phys. Today* 60:51–57
80. Krogh-Madsen T, Christini D. 2012. *Annu. Rev. Biomed. Eng.* 14:179–203
81. Courtemanche M, Glass L, Keener J. 1993. *Phys. Rev. Lett.* 70:2182–85
82. Cross MC, Hohenberg PC. 1993. *Rev. Mod. Phys.* 65:851–1112
83. Restrepo JG, Karma A. 2009. *Phys. Rev. E*. 79:030906R
84. Chudin E, Goldhaber J, Garfinkel A, Weiss J, Kogan B. 1999. *Biophys. J.* 77:2930–41
85. Diaz ME, O'Neill SC, Eisner DA. 2004. *Circ. Res.* 94:650–56
86. Picht E, DeSantiago J, Blatter LA, Bers DM. 2006. *Circ. Res.* 99:740–48
87. Laurita KR, Rosenbaum DS. 2008. *Prog. Biophys. Mol. Biol.* 97:332–47
88. Aistrup GL, Shiferaw Y, Kapur S, Kadish AH, Wasserstrom JA. 2009. *Circ. Res.* 104:639–49
89. Wan X, Cutler M, Song Z, Karma A, Matsuda T, et al. 2012. *Heart Rhythm* 9:1698–1705
90. Kockskämper J, Blatter LA. 2002. *J. Physiol.* 545:65–79
91. Xie L-H, Weiss JN. 2009. *Am. J. Physiol. Heart Circ. Physiol.* 297:997–1002
92. Gaeta SA, Bub G, Abbott GW, Christini DJ. 2009. *Circ. Res.* 105:335–42
93. Geisse NA, Sheehy SP, Parker KK. 2009. *In Vitro Cell. Dev. Biol. Anim.* 45:343–50
94. Rovetti R, Das KK, Garfinkel A, Shiferaw Y. 2007. *Phys. Rev. E*. 76:051920
95. Shiferaw Y, Karma A. 2006. *Proc. Natl. Acad. Sci. USA* 103:5670–75
96. Turing AM. 1952. *Philos. Trans. R. Soc. Lond. Ser. B* 237:37–72
97. Gierer A, Meinhardt H. 1972. *Biol. Cybern.* 12:30–39
98. Gaeta SA, Krogh-Madsen T, Christini DJ. 2010. *J. Theor. Biol.* 266:408–18
99. Karma A. 1993. *Phys. Rev. Lett.* 71:1103–6
100. Karma A. 1994. *Chaos* 4:461–72
101. Qu Z, Xie F, Garfinkel A, Weiss JN. 2000. *Ann. Biomed. Eng.* 28:755–71
102. Fenton FH, Cherry EM, Hastings HM, Evans SJ. 2002. *Chaos* 12:852–91
103. Fenton F, Karma A. 1998. *Phys. Rev. Lett.* 81:481–84
104. Fenton F, Karma A. 1998. *Chaos* 8:20–47
105. Rappel WJ. 2001. *Chaos* 11:71–80
106. Qu Z, Kil J, Xie F, Garfinkel A, Weiss JN. 2000. *Biophys. J.* 78:2761–75
107. Keldermann RH, ten Tusscher KH, Nash MP, Bradley CP, Hren R, et al. 2009. *Am. J. Physiol. Heart Circ. Physiol.* 296(2):H370–79
108. Winfree AT. 1994. *Science* 266:1003–6
109. Alonso S, Panfilov AV. 2008. *Phys. Rev. Lett.* 100:218101
110. Henze C, Lugosi E, Winfree AT. 1990. *Can. J. Phys.* 68:683–710
111. Henry H, Hakim V. 2000. *Phys. Rev. Lett.* 85:5328–31
112. Henry H, Hakim V. 2002. *Phys. Rev. E*. 65:046235
113. Echebarria B, Hakim V, Henry H. 2006. *Phys. Rev. Lett.* 96:098301
114. Setayeshgar S, Bernoff AJ. 2002. *Phys. Rev. Lett.* 88:028101
115. Vershelde H, Dierckx H, Bernus O. 2007. *Phys. Rev. Lett.* 99:168104
116. Ripplinger CM, Li W, Hadley J, Chen J, Rothenberg F, et al. 2007. *Circ. Res.* 101:1049–57
117. Tran DX, Sato D, Yochelis A, Weiss JN, Garfinkel A, Qu Z. 2009. *Phys. Rev. Lett.* 102:258103
118. Sato D, Xie L-H, Sovari AA, Tran DX, Morita N, et al. 2009. *Proc. Natl. Acad. Sci. USA* 106:2983–88
119. Weiss JN, Garfinkel A, Karagueuzian HS, Chen PS, Qu Z. 2010. *Heart Rhythm* 7:1891–99
120. Odening KE, Choi B-R, Liu GX, Hartmann K, Ziv OO, et al. 2012. *Heart Rhythm* 9:823–32
121. Christini DJ, Stein KM, Markowitz SM, Mittal S, Slotwiner DJ, et al. 2001. *Proc. Natl. Acad. Sci. USA* 98:5827–32
122. Hall GM, Gauthier DJ. 2002. *Phys. Rev. Lett.* 88:198102
123. Rappel W-J, Fenton F, Karma A. 1999. *Phys. Rev. Lett.* 83:456–59
124. Echebarria B, Karma A. 2002. *Chaos* 12:923–30

125. Christini DJ, Riccio ML, Culianu CA, Fox JJ, Karma A, Gilmour RF. 2006. *Phys. Rev. Lett.* 96:1–4
126. Krogh-Madsen T, Karma A, Riccio ML, Jordan PN, Christini DJ, Gilmour RF. 2010. *Phys. Rev. E.* 81: 1–7
127. Garzon A, Roman OG, Fenton FH. 2011. *Phys. Rev. E.* 80:021932
128. Garzon A, Roman OG, Fenton FH. 2011. *Phys. Rev. E.* 84:041927
129. Ripplinger CM, Krinsky VI, Nikolski VP, Efimov IR. 2006. *Am. J. Physiol. Heart Circ. Physiol.* 291: H184–92
130. Pumir A, Nikolski V, Horning M, Isomura A, Agladze K, et al. 2007. *Phys. Rev. Lett.* 99:208101
131. Fenton FH, Luther S, Cherry EM, Otani NF, Krinsky V, et al. 2009. *Circulation* 120:467–76
132. Luther S, Fenton FH, Kornreich BG, Squires A, Bittihn P, et al. 2011. *Nature* 475:235–39
133. Wenwen L, Janardhan AH, Fedorov VV, Qun S, Schuessler RB, Efimov IR. 2011. *Arrhythm. Electrophysiol.* 4:917–25
134. Sobie EA. 2009. *Biophys. J.* 96:1264–74
135. Sarkar AX, Sobie EA. 2010. *PLOS Comput. Biol.* 6:e1000914
136. Kherlopian A, Ortega F, Christini DJ. 2011. *Genet. Evol. Comput.* 2011:755–58
137. Weiss JN, Karma A, MacLellan WR, Deng M, Rau CD, et al. 2012. *Circ. Res.* 111:493–504



Contents

Why I Haven't Retired <i>Theodore H. Geballe</i>	1
Quantum Control over Single Spins in Diamond <i>V.V. Dobrovitski, G.D. Fuchs, A.L. Falk, C. Santori, and D.D. Awschalom</i>	23
Prospects for Spin-Based Quantum Computing in Quantum Dots <i>Christoph Kloeffel and Daniel Loss</i>	51
Quantum Interfaces Between Atomic and Solid-State Systems <i>Nikos Daniilidis and Hartmut Häffner</i>	83
Search for Majorana Fermions in Superconductors <i>C.W.J. Beenakker</i>	113
Strong Correlations from Hund's Coupling <i>Antoine Georges, Luca de' Medici, and Jernej Mravlje</i>	137
Bridging Lattice-Scale Physics and Continuum Field Theory with Quantum Monte Carlo Simulations <i>Ribhu K. Kaul, Roger G. Melko, and Anders W. Sandvik</i>	179
Colloidal Particles: Crystals, Glasses, and Gels <i>Peter J. Lu (陸述義) and David A. Weitz</i>	217
Fluctuations, Linear Response, and Currents in Out-of-Equilibrium Systems <i>S. Ciliberto, R. Gomez-Solano, and A. Petrosyan</i>	235
Glass Transition Thermodynamics and Kinetics <i>Frank H. Stillinger and Pablo G. Debenedetti</i>	263
Statistical Mechanics of Modularity and Horizontal Gene Transfer <i>Michael W. Deem</i>	287

Physics of Cardiac Arrhythmogenesis	
<i>Alain Karma</i>	313
Statistical Physics of T-Cell Development and Pathogen Specificity	
<i>Andrej Košmrlj, Mehran Kardar, and Arup K. Chakraborty</i>	339

Errata

An online log of corrections to *Annual Review of Condensed Matter Physics* articles may be found at <http://conmatphys.annualreviews.org/errata.shtml>